LETTER

doi:10.1038/nature14896

Structural basis for stop codon recognition in eukaryotes

Alan Brown[1]*, Sichen Shao[1]*, Jason Murray[1], Ramanujan S. Hegde[1] & V. Ramakrishnan[1]

Termination of protein synthesis occurs when a translating ribosome encounters one of three universally conserved stop codons: UAA, UAG or UGA. Release factors recognize stop codons in the ribosomal A-site to mediate release of the nascent chain and recycling of the ribosome. Bacteria decode stop codons using two separate release factors with differing specificities for the second and third bases[1]. By contrast, eukaryotes rely on an evolutionarily unrelated omnipotent release factor (eRF1) to recognize all three stop codons[2]. The molecular basis of eRF1 discrimination for stop codons over sense codons is not known. Here we present cryo-electron microscopy (cryo-EM) structures at 3.5–3.8 Å resolution of mammalian ribosomal complexes containing eRF1 interacting with each of the three stop codons in the A-site. Binding of eRF1 flips nucleotide A1825 of 18S ribosomal RNA so that it stacks on the second and third stop codon bases. This configuration pulls the fourth position base into the A-site, where it is stabilized by stacking against G626 of 18S rRNA. Thus, eRF1 exploits two rRNA nucleotides also used during transfer RNA selection to drive messenger RNA compaction. In this compacted mRNA conformation, stop codons are favoured by a hydrogen-bonding network formed between rRNA and essential eRF1 residues that constrains the identity of the bases. These results provide a molecular framework for eukaryotic stop codon recognition and have implications for future studies on the mechanisms of canonical and premature translation termination[3,4].

Termination of translation in eukaryotes is initiated when a ternary complex of eRF1–eRF3–GTP binds to a stop codon in the ribosomal A-site[5,6]. GTP hydrolysis by eRF3 induces a conformational change that leads to its dissociation, permitting eRF1 to accommodate fully in the A-site. This change is thought to bring a universally conserved GGQ motif close to the ester bond between the nascent polypeptide and the tRNA, stimulating its hydrolysis. Concomitant with these events, the ATPase ABCE1 is recruited to the ribosome after eRF3 dissociation and, together with eRF1, catalyses splitting of the ribosomal subunits to recycle post-termination complexes[3,4,7,8].

We reasoned that a catalytically inactive eRF1 mutant may trap a pre-hydrolysis termination complex with two key features. First, eRF1 would be in complex with the stop codon it had recognized. Second, the unreleased nascent polypeptide would provide a unique affinity handle to enrich this species for structural analysis. Therefore, we substituted the glycines of the GGQ motif with alanines (eRF1(AAQ))[9] and added this mutant to *in vitro* translation reactions in rabbit reticulocyte lysate. Peptide release at all three stop codons was inhibited by eRF1(AAQ) as judged by persistence of a peptidyl-tRNA (Extended Data Fig. 1a, b). Affinity purification of these ribosome-nascent chain complexes (RNCs) via the nascent chain recovered both eRF1(AAQ) and ABCE1 (Extended Data Fig. 1c, d), suggesting that eRF1(AAQ) was trapped on the RNCs in its accommodated state. Association of ABCE1 was enhanced with eRF1(AAQ)-stalled RNCs relative to RNCs stalled with a truncated mRNA (Extended Data Fig. 1c), consistent with a report that the function of ABCE1 in post-termination recycling requires peptidyl-tRNA hydrolysis[7].

Purified RNCs stalled with eRF1(AAQ) at each stop codon (Extended Data Fig. 1d) were directly used for cryo-EM. Multiple rounds of three-dimensional classification *in silico* revealed that ~10% of the particles contained eRF1(AAQ)–ABCE1 (Extended Data Fig. 2).

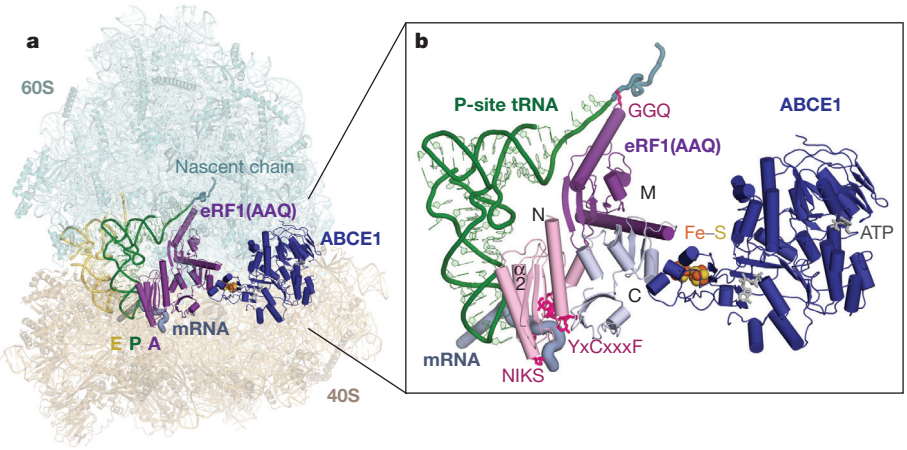

Figure 1 | Overall structure of a eukaryotic translation termination complex. **a**, Overview of the eRF1(AAQ)-stalled mammalian ribosome-nascent chain complex containing the UAG stop codon. Displayed are the 40S and 60S ribosomal subunits, E- and P-site tRNAs, eRF1(AAQ) occupying the A-site, and ABCE1 occupying the GTPase centre. **b**, Close-up view of eRF1(AAQ) coloured by domain (N, M, C) with the GGQ, NIKS and YxCxxxF motifs highlighted (pink). Also shown are the P-site tRNA, nascent polypeptide, the mRNA containing the UAG stop codon, and ABCE1 with its iron–sulfur clusters and nucleotide-binding sites indicated.

[1]MRC Laboratory of Molecular Biology, Francis Crick Avenue, Cambridge CB2 0QH, UK.
*These authors contributed equally to this work

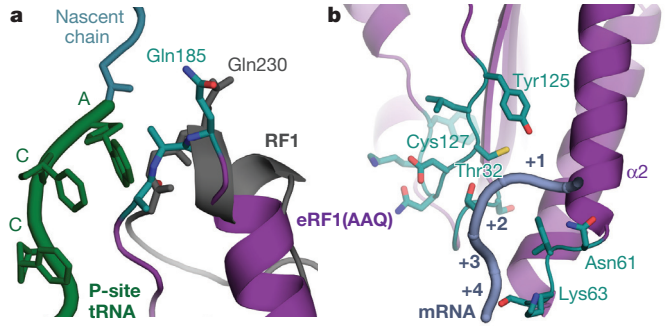

Figure 2 | Conformation of essential eRF1 motifs. **a**, Conformation of the GGQ-loop (teal) of eRF1(AAQ) (purple) within the peptidyl transferase centre. The AAQ tripeptide, positioned next to the CCA end of the P-site tRNA (green), closely resembles the conformation adopted by GGQ of a bacterial release factor (RF1, grey) bound to the ribosome. **b**, Positions of NIKS, YxCxxxF, and GTS (teal) motifs in the N domain of eRF1(AAQ) (purple) relative to the mRNA (slate). The positions of the stop codon (+1 to +3) and the following base (+4) are indicated.

Data sets of between 20,000 and 50,000 particles for the three stop codons yielded maps with overall resolutions of 3.65 Å (UAA), 3.45 Å (UAG) and 3.83 Å (UGA), against which the models were refined (Fig. 1, Extended Data Fig. 3 and Extended Data Table 1).

In each reconstruction, eRF1 is in its extended conformation[10], and ABCE1 occupies the GTPase centre (Fig. 1a). The three domains of eRF1 (N, M and C) have moved relative to one another compared to the crystal structure[11] (Extended Data Fig. 4a) and are each well resolved (Extended Data Fig. 3b). Direct interactions of the N domain with the codon deep in the decoding centre argues against an earlier suggestion that eRF1 disengages from the stop codon in the presence of ABCE1 (ref. 10).

The N and M domains of eRF1 independently contact the P-site tRNA and together structurally resemble a tRNA in the A-site (Fig. 1b). Helix α2 of the N domain runs parallel to, and interacts with, the anticodon stem-loop of the P-site tRNA (Extended Data Fig. 4b). The M domain is functionally analogous to the tRNA acceptor stem[11], and positions the GGQ motif[9] in the peptidyl transferase centre (Fig. 1b). To occupy a similar position as the 3′ end of an A-site tRNA, the GGQ-loop is shifted by 10 Å compared to the crystal structure[11] (Extended Data Fig. 4c). This positions the alanine residues of the mutated GGQ motif directly opposite the terminal 3′ adenosine of the P-site tRNA and the glutamine (Gln185) in proximity to the ester bond between the nascent polypeptide and the tRNA. This conformation closely resembles that of the GGQ-loop in bacterial release factors[12–14] (Fig. 2a).

At the decoding centre, the interactions between the N domain of eRF1 and the stop codon are well resolved (Fig. 2b and Extended Data Fig. 5). The most striking feature is a compact configuration of mRNA that accommodates four nucleotides in the A-site instead of three (Fig. 3a, b). mRNA compaction depends crucially on the 'flipping out' of A1825 (A1493 in bacteria) in helix 44 (h44) of 18S rRNA, forming a stacking interaction with the +2 nucleotide of the stop codon, on which the +3 nucleotide stacks. This configuration allows the +4 nucleotide to stack with base G626 (G530 in bacteria) of 18S rRNA (Fig. 3b). Stacking with G626 would be more stable for purines, explaining their statistical bias at the +4 position in eukaryotes[15]. Compaction of mRNA in the A-site probably results in pulling downstream mRNA further into the mRNA channel. This is consistent with protection of two additional nucleotides of 3′ mRNA upon eRF1 binding to the ribosome[16,17].

The structures of the bacterial release factor complexes are qualitatively distinct (Fig. 3c). Instead of A1493, the adjacent A1492 is flipped out[12–14]. However, this flipped base does not stack with any of the stop codon bases and does not lead to mRNA compaction. G530 therefore stacks with the +3 base of the stop codon[12–14] instead of the +4 base. While the +4 base also affects stop codon recognition in bacteria, the greatest preference seems to be for uridine rather than for purines[18]. Thus, eukaryotes seem to exploit the +4 base to stabilize mRNA compaction. The unique stacking of the +2 and +3 bases in this compacted state is an important element for stop codon recognition by eRF1 (see below).

The conserved NIKS, YxCxxxF and GTS motifs in eRF1 have been crosslinked to stop codon bases[19,20]. In the structures here, the essential NIKS sequence (residues 61–64)[21], located at the end of helix α2, imposes a requirement for uridine in the first (+1) position via interactions with its Watson–Crick edge. A local distortion in helix α2 and the subsequent loop helps to optimise hydrogen-bond interactions with the nucleotide (Fig. 4a). The side chains of Asn61 and Lys63 are within hydrogen-bonding distance of the uracil carbonyl groups. A further hydrogen bond may form with the main chain carbonyl of

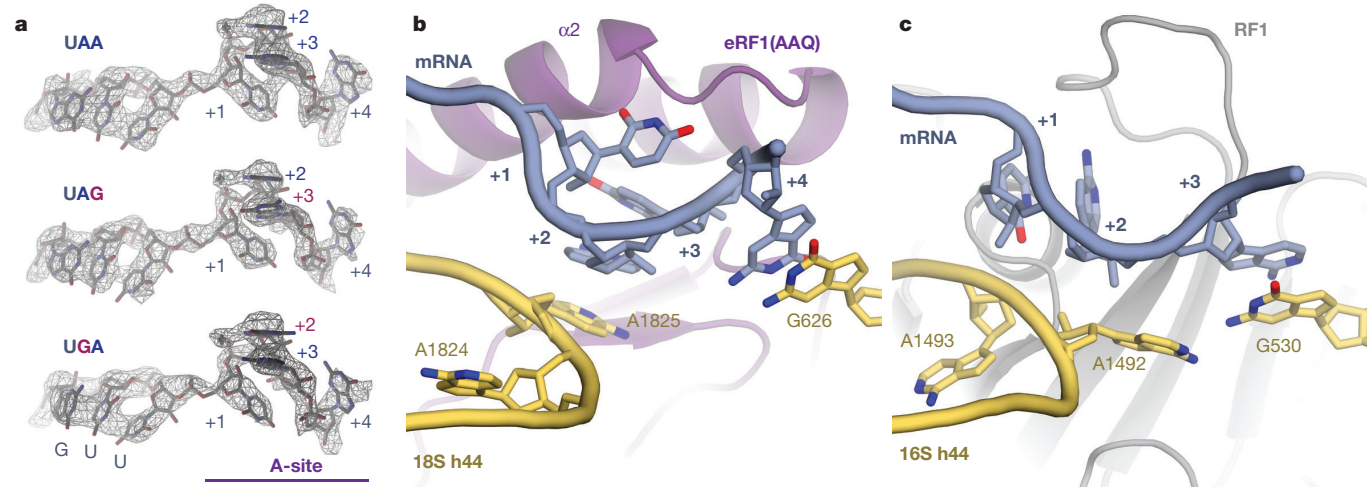

Figure 3 | Stop codon configuration in the eukaryotic decoding centre. **a**, Electron microscopy map densities (contoured at 0.12–0.17 e Å^{-3}) of the mRNA in each termination complex reveal the same compacted conformation. The P-site Val^{GUU} codon and the stop codon (+1 to +3) and following base (+4) in the A-site are indicated. **b**, eRF1(AAQ) (purple) recognizes four mRNA bases (+1 to +4, slate) in the A-site. Bases +2 and +3 stack on A1825, which is flipped out of helix 44 (h44), and base +4 on G626 of 18S rRNA. **c**, In bacteria, RF1 (grey) recognizes a more extended stop codon configuration where the +3 base stacks on G530 (the equivalent of G626) of 16S rRNA.

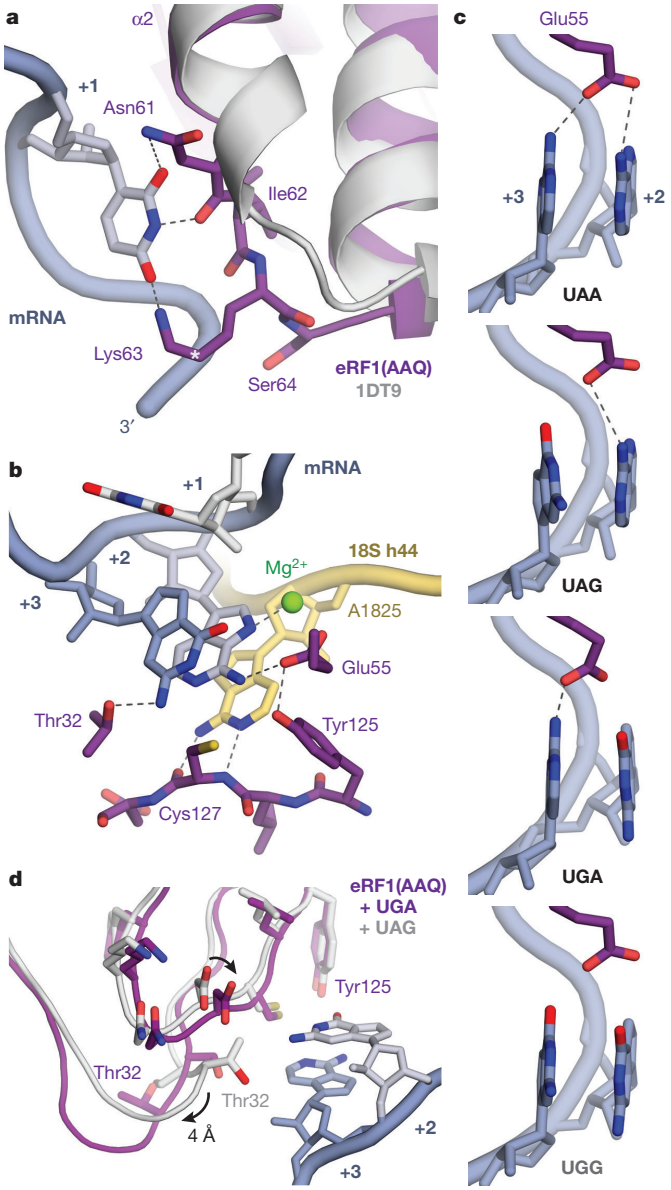

Figure 4 | Molecular basis of stop codon recognition by eRF1. **a**, Comparison of ribosome-bound eRF1(AAQ) (purple) relative to the eRF1 crystal structure (PDB accession code 1DT9, light grey) shows how the NIKS motif hydrogen bonds with the +1 uridine (slate) of stop codons. Hydroxylation of Lys63 occurs on Cδ (*). **b**, Interaction network of the UAG stop codon (slate) with eRF1(AAQ) (purple) and A1825 of 18S rRNA (yellow). Interactions proposed to stabilize the flipped out position of A1825 and its stacking with the +2 and +3 bases are indicated by dotted lines. **c**, Model for stop codon discrimination by eRF1. Glu55 of eRF1(AAQ) (purple) would hydrogen bond with the stacked +2 and +3 bases (slate) of stop codons but not the sense codon UGG. **d**, Comparison of UGA-bound eRF1(AAQ) (purple) relative to UAG-bound eRF1(AAQ) (white).

Asn61. Hydroxylation of Lys63 (at the Cδ position) reduces stop codon read-through and promotes peptide release *in vivo*[22]. The hydroxyl group may allow an additional interaction with the phosphate backbone of the mRNA and help position the ε-amino group for optimal hydrogen bonding.

Purines would be disfavoured at the +1 position by steric hindrance with eRF1, while cytidine would be incompatible with the hydrogen-bonding requirements of the NIKS motif (Extended Data Fig. 6). Thus, the universality of uridine in the first position of stop codons is defined by extensive hydrogen bonding with eRF1. In bacteria, RF1 and RF2 also utilize hydrogen-bonding networks to specify uridine in the +1 position, but with different interactions[12], highlighting how independent solutions have evolved for the same specificity problem.

Interactions of the YxCxxxF motif and Glu55 of eRF1 with the +2 and +3 purines provide a basis for stop codon discrimination from sense codons (Fig. 4b, c). The main chain of Cys127 from the YxCxxxF motif can form two hydrogen bonds with the Watson–Crick edge of A1825 to stabilize its flipped orientation, facilitating stacking of the +2 and +3 bases (Fig. 4b). The invariant residues Glu55 from helix α2 and Tyr125 may act as a pair[23] to position the glutamate side chain so that it can hydrogen bond with the N6 atoms of adenosines at the +2 and/or +3 positions. These interactions are only possible with purines, excluding pyrimidines from the +2 and +3 positions in stop codons. In the case of UGG, which codes for tryptophan, the two O6 atoms of consecutive stacked guanosines would not satisfy the hydrogen-bonding requirements, and their increased repulsion with each other and with the negatively-charged Glu55 would also disfavour the formation of the conformation that allows these interactions (Fig. 4c).

The conserved GTS motif, located towards the sugar edge of the +3 base, adopts two different conformations that are interdependent with the position of the YxCxxxF motif[24]. With adenosine in the +2 position, Thr32 faces the +3 base and can hydrogen bond with the N2 atom of the guanosine in UAG (Fig. 4b). A guanosine at the +2 position is accommodated by a movement of the YxCxxxF motif towards the stacked pair by ~1 Å, which propagates a 4 Å movement of the GTS motif so that Thr32 now faces away from the stop codon (Fig. 4d). Consistent with these observations, perturbation of any residue contributing to this network has substantial effects on stop codon recognition and specificity[17,23,25,26].

In conclusion, these structures show how stop codons are specifically selected by eRF1. At the +1 position, only uridine can form the network of interactions with the NIKS motif. The flipping of A1825 results in its stacking onto the +2 and +3 bases of a distorted mRNA so that they are decoded as a single unit (Fig. 4b). This solves the puzzle of how guanosine can occur at either the +2 or +3 position but not at both: two successive guanosines would lead to repulsion between their O6 atoms and with Glu55 (Fig. 4c). By requiring two purines while specifically excluding consecutive guanosines, the selectivity of eRF1 at the +2 and +3 positions is logically equivalent to a NAND gate.

This mechanism for stop codon recognition by eRF1 is distinct from that used by the evolutionarily and structurally unrelated bacterial release factors, even though they share some common strategies including the extensive use of hydrogen bonding for decoding specificity and an invariant GGQ motif to catalyse peptide hydrolysis. The work here paves the way for studies on the mechanism of termination and ribosome recycling, including the roles of eRF3 and ABCE1, as well as the interaction of termination factors with quality control pathways such as nonsense-mediated mRNA decay[27]. Finally, insight into stop codon recognition can provide a framework for the development of inhibitors of termination that may be useful to treat the ~11% of hereditary diseases caused by premature termination[28,29].

Online Content Methods, along with any additional Extended Data display items and Source Data, are available in the online version of the paper; references unique to these sections appear only in the online paper.

Received 30 April; accepted 9 July 2015.
Published online 5 August 2015.

1. Scolnick, E., Tompkins, R., Caskey, T. & Nirenberg, M. Release factors differing in specificity for terminator codons. *Proc. Natl Acad. Sci. USA* **61,** 768–774 (1968).
2. Frolova, L. *et al.* A highly conserved eukaryotic protein family possessing properties of polypeptide chain release factor. *Nature* **372,** 701–703 (1994).
3. Dever, T. E. & Green, R. The elongation, termination, and recycling phases of translation in eukaryotes. *Cold Spring Harb. Perspect. Biol.* **4,** a013706 (2012).
4. Jackson, R. J., Hellen, C. U. T. & Pestova, T. V. Termination and post-termination events in eukaryotic translation. *Adv. Protein Chem. Struct. Biol.* **86,** 45–93 (2012).
5. Muhs, M. *et al.* Cryo-EM of ribosomal 80S complexes with termination factors reveals the translocated cricket paralysis virus IRES. *Mol. Cell* **57,** 422–432 (2015).

6. Taylor, D. *et al.* Cryo-EM structure of the mammalian eukaryotic release factor eRF1–eRF3-associated termination complex. *Proc. Natl Acad. Sci. USA* **109,** 18413–18418 (2012).
7. Pisarev, A. V. *et al.* The role of ABCE1 in eukaryotic posttermination ribosomal recycling. *Mol. Cell* **37,** 196–210 (2010).
8. Shoemaker, C. J. & Green, R. Kinetic analysis reveals the ordered coupling of translation termination and ribosome recycling in yeast. *Proc. Natl Acad. Sci. USA* **108,** E1392–E1398 (2011).
9. Frolova, L. Y. *et al.* Mutations in the highly conserved GGQ motif of class 1 polypeptide release factors abolish ability of human eRF1 to trigger peptidyl-tRNA hydrolysis. *RNA* **5,** 1014–1020 (1999).
10. Preis, A. *et al.* Cryoelectron microscopic structures of eukaryotic translation termination complexes containing eRF1-eRF3 or eRF1-ABCE1. *Cell Rep.* **8,** 59–65 (2014).
11. Song, H. *et al.* The crystal structure of human eukaryotic release factor eRF1—mechanism of stop codon recognition and peptidyl-tRNA hydrolysis. *Cell* **100,** 311–321 (2000).
12. Laurberg, M. *et al.* Structural basis for translation termination on the 70S ribosome. *Nature* **454,** 852–857 (2008).
13. Weixlbaumer, A. *et al.* Insights into translational termination from the structure of RF2 bound to the ribosome. *Science* **322,** 953–956 (2008).
14. Korostelev, A. *et al.* Crystal structure of a translation termination complex formed with release factor RF2. *Proc. Natl Acad. Sci. USA* **105,** 19684–19689 (2008).
15. Brown, C. M., Stockwell, P. A., Trotman, C. N. & Tate, W. P. Sequence analysis suggests that tetra-nucleotides signal the termination of protein synthesis in eukaryotes. *Nucleic Acids Res.* **18,** 6339–6345 (1990).
16. Shirokikh, N. E. *et al.* Quantitative analysis of ribosome–mRNA complexes at different translation stages. *Nucleic Acids Res.* **38,** e15 (2010).
17. Kryuchkova, P. *et al.* Two-step model of stop codon recognition by eukaryotic release factor eRF1. *Nucleic Acids Res.* **41,** 4573–4586 (2013).
18. Poole, E. S., Brown, C. M. & Tate, W. P. The identity of the base following the stop codon determines the efficiency of *in vivo* translational termination in *Escherichia coli*. *EMBO J.* **14,** 151–158 (1995).
19. Chavatte, L., Seit-Nebi, A., Dubovaya, V. & Favre, A. The invariant uridine of stop codons contacts the conserved NIKSR loop of human eRF1 in the ribosome. *EMBO J.* **21,** 5302–5311 (2002).
20. Bulygin, K. N. *et al.* Three distinct peptides from the N domain of translation termination factor eRF1 surround stop codon in the ribosome. *RNA* **16,** 1902–1914 (2010).
21. Frolova, L., Seit-Nebi, A. & Kisselev, L. Highly conserved NIKS tetrapeptide is functionally essential in eukaryotic translation termination factor eRF1. *RNA* **8,** 129–136 (2002).
22. Feng, T. *et al.* Optimal translational termination requires C4 lysyl hydroxylation of eRF1. *Mol. Cell* **53,** 645–654 (2014).
23. Kolosov, P. *et al.* Invariant amino acids essential for decoding function of polypeptide release factor eRF1. *Nucleic Acids Res.* **33,** 6418–6425 (2005).
24. Wong, L. E., Li, Y., Pillay, S., Frolova, L. & Pervushin, K. Selectivity of stop codon recognition in translation termination is modulated by multiple conformations of GTS loop in eRF1. *Nucleic Acids Res.* **40,** 5751–5765 (2012).
25. Cheng, Z. *et al.* Structural insights into eRF3 and stop codon recognition by eRF1. *Genes Dev.* **23,** 1106–1118 (2009).
26. Seit-Nebi, A., Frolova, L. & Kisselev, L. Conversion of omnipotent translation termination factor eRF1 into ciliate-like UGA-only unipotent eRF1. *EMBO Rep.* **3,** 881–886 (2002).
27. Czaplinski, K. *et al.* The surveillance complex interacts with the translation release factors to enhance termination and degrade aberrant mRNAs. *Genes Dev.* **12,** 1665–1677 (1998).
28. Keeling, K. M., Xue, X., Gunn, G. & Bedwell, D. M. Therapeutics based on stop codon readthrough. *Annu. Rev. Genomics Hum. Genet.* **15,** 371–394 (2014).
29. Mort, M., Ivanov, D., Cooper, D. N. & Chuzhanova, N. A. A meta-analysis of nonsense mutations causing human genetic disease. *Hum. Mutat.* **29,** 1037–1047 (2008).

Acknowledgements We thank C. Savva, F. de Haas, and S. Welsch for assisting with cryo-EM data collection, J. Grimmett and T. Darling for computing support, D. Barford for critically reading the manuscript, and I. Fernández, J. Llácer, G. Murshudov, S. Scheres, and R. Voorhees for useful discussions. Gctf is available on request from K. Zhang (kzhang@mrc-lmb.cam.ac.uk). This work was supported by the UK Medical Research Council (MC_UP_A022_1007 to R.S.H. and MC_U105184332 to V.R.). A.B. was supported by a Career Development Fellowship. S.S. was supported by a St John's College Title A fellowship. J.M. thanks T. Dever, NICHD, and the NIH Oxford-Cambridge Scholars' Program for support. V.R. was supported by a Wellcome Trust Senior Investigator award (WT096570), the Agouron Institute, and the Jeantet Foundation.

Author Contributions A.B., S.S., R.S.H. and V.R. designed the study. S.S. purified complexes and prepared samples. A.B., S.S. and J.M. collected data. A.B. calculated the cryo-EM reconstructions, built the atomic models and interpreted the structure. A.B., S.S., R.S.H and V.R. wrote the manuscript. All authors discussed and commented on the final manuscript.

Author Information Maps have been deposited with the EMDB under accession codes 3038, 3039, and 3040. Atomic coordinates have been deposited with the Protein Data Bank under accession codes 3JAG, 3JAH and 3JAI. Reprints and permissions information is available at www.nature.com/reprints. The authors declare no competing financial interests. Readers are welcome to comment on the online version of the paper. Correspondence and requests for materials should be addressed to R.S.H. (rhegde@mrc-lmb.cam.ac.uk) or V.R. (ramak@mrc-lmb.cam.ac.uk).

METHODS

No statistical methods were used to predetermine sample size and the experiments were not randomized.

Plasmids and antibodies. An SP64-based plasmid encoding 3 × Flag-tagged Sec61β containing the autonomously-folding villin headpiece (VHP) domain[30] was modified by individually inserting each stop codon (TAA, TAG, TGA) after the valine at position 68 of unmodified Sec61β. The remaining carboxy-terminal portion of the protein was deleted using Phusion mutagenesis (Thermo Scientific). *In vitro* transcription reactions were performed using PCR products generated with primers flanking the SP6 promoter and the 3′ UTR of the SP64 vector as previously described[31]. The complementary DNA encoding human eRF1 (Origene) was subcloned into a pRSETA expression vector after an amino-terminal 6 × His tag and tobacco etch virus (TEV) cleavage site using standard procedures. The eRF1(AAQ) mutant was generated via Phusion mutagenesis. Antibodies against Hbs1 and ABCE1 have been described[32]; the eRF1 antibody was from New England Biolabs.

Release factor purification. Wild-type and mutant eRF1 (eRF1(AAQ)) were expressed in and purified from *Escherichia coli* BL21(DE3) cells grown under antibiotic selection in LB. Transformed cells were induced at $A_{600\ nm} = 0.4–0.6$ with 0.2 mM IPTG for 2 h at 37 °C and lysed with a microfluidiser in lysis buffer (1 × PBS, pH 7.5, 250 mM NaCl, 10 mM imidazole, 1 mM DTT) containing 1 × protease inhibitor cocktail (Roche). Lysates were clarified by centrifugation and the supernatant passed over a NiNTA column. After washing with 25 column volumes of lysis buffer, elutions were carried out with 250 mM imidazole in lysis buffer. Peak fractions were pooled, dialysed overnight in the presence of TEV protease against 50 mM HEPES, pH 7.4, 150 mM potassium acetate, 5 mM magnesium diacetate, 10 mM imidazole, 10% glycerol, 1 mM DTT. The TEV protease and cleaved His tag were removed by passage over a NiNTA column.

***In vitro* translations and sample preparation.** *In vitro* translations in a rabbit reticulocyte (RRL) system were for 25 min at 32 °C as described previously[30,31]. Where indicated, 0.5 μM eRF1(AAQ) was included to trap termination complexes. 4 ml translation reactions were directly incubated with 100 μl (packed volume) of anti-Flag M2 beads (Sigma) for 1–1.5 h at 4 °C with gentle mixing. The beads were washed sequentially with 6 ml of 50 mM HEPES, pH 7.4, 100 mM potassium acetate, 5 mM magnesium diacetate, 0.1% Triton X-100, 1 mM DTT, 6 ml of 50 mM HEPES, pH 7.4, 250 mM potassium acetate, 5 mM magnesium diacetate, 0.5% Triton X-100, 1 mM DTT and 6 ml of RNC buffer (50 mM HEPES, pH 7.4, 100 mM potassium acetate, 5 mM magnesium diacetate, 1 mM DTT). Two sequential elutions were carried out with 100 μl 0.1 mg ml^{-1} 3 × Flag peptide (Sigma) in RNC buffer at room temperature for 25 min. The elutions were combined and centrifuged at 100,000 rpm at 4 °C for 40 min in a TLA120.2 rotor (Beckman Coulter) before resuspension of the ribosomal pellet in RNC buffer.

Electron microscopy. 3 μl aliquots of purified ribosome complexes at a concentration of 120 nM were applied onto Quantifoil R2/2 cryo-EM grids covered with continuous carbon (estimated to be 50 Å thick) at 4 °C and 100% ambient humidity. After 30 s incubation, the grids were blotted for 3 s and vitrified in liquid ethane using a Vitrobot MKIII (FEI).

Automated data collection (EPU software, FEI) was conducted on a Titan Krios microscope equipped with a XFEG electron source using 300 kV acceleration voltage. For each 1.1 s exposure, 17 movie frames were recorded on a Falcon II direct electron detector (FEI) at a calibrated magnification of 104,478, resulting in a pixel size of 1.34 Å (ref. 33). A dose rate of ~30 electrons per $Å^2$ per second was used. Defocus values ranged from −1.1 to −5.9 μm for the UAA-eRF1(AAQ) data set, −0.7 to −4.1 μm for the UAG-eRF1(AAQ) data set, and −0.7 to −3.8 μm for the UGA-eRF1(AAQ) data set (Extended Data Table 1), as more images were collected closer to focus on the latter two data sets.

Image processing. The 17 frames were aligned using whole-image motion correction[34] to reduce beam-induced blurring of the images. Parameters of the contrast transfer function for each motion-corrected micrograph were obtained using Gctf (K. Zhang (kzhang@mrc-lmb.cam.ac.uk), MRC-LMB, in development). Ribosome particles were selected using semi-automated particle picking implemented in RELION[35]. All two- and three-dimensional classifications and refinements were performed using RELION[36]. We used reference-free two-dimensional class averaging to discard non-ribosomal particles and three-dimensional classification to sort different compositions and conformations of the ribosome complexes. After two-dimensional classification, the UAA-eRF1(AAQ) data set contained 556,994 particles from two independent data acquisitions, while the UAG-eRF1(AAQ) and UGA-eRF1(AAQ) data sets contained 216,276 and 250,705 particles, respectively, both from a single data acquisition.

A 40 Å low-pass filtered cryo-EM reconstruction of the rabbit 80S ribosome (Electron Microscopy Data Bank (EMDB) accession 2704)[32] was used as an initial model for the three-dimensional refinement. In a subsequent three-dimensional classification run with 12 classes, an angular sampling of 1.8° was combined with local angular searches, and the refined model from the first refinement was used as a starting model. A further round of refinement and three-dimensional classification into 6 classes using an angular sampling of 0.9° combined with local angular searches was necessary to isolate a homogeneous class of ribosomes bound with eRF1–ABCE1 (see Extended Data Fig. 2). This resulted in 49,979 particles for the UAA–eRF1(AAQ) data set, 20,515 particles for the UAG–eRF1(AAQ) data set, and 22,058 particles for the UGA–eRF1(AAQ) data set.

Prior to a final round of refinement and classification with classes combined from different data sets, statistical particle-based movie correction was performed in RELION-1.4. For these calculations we used running averages of five movie frames, and a standard deviation of one pixel for the translational alignment. In addition, we used a resolution and dose-dependent model for the radiation damage, in which each frame is B-factor weighted as estimated from single-frame reconstructions[37].

Reported resolutions are based on the Fourier shell correlation (FSC) 0.143 criterion. High-resolution noise substitution was used to correct for the effects of a soft mask on FSC curves[38]. Before visualization, density maps were corrected for the modulation transfer function of the Falcon II detector and then sharpened by applying a negative B-factor that was estimated using automated procedures[39] (Extended Data Table 1). Local resolution was quantified using ResMap[40].

Model building. The reconstruction was initially interpreted by docking the large and small subunits of the mammalian 80S ribosome, with respective Protein Data Bank (PDB) accession codes 3J92 and 3J7P[41,42], into the map using Chimera[43]. The crystal structures of human eRF1 (PDB accession code 1DT9)[11] and *Pyrococcus abysii* ABCE1 (PDB accession code 3BK7)[44] were docked into the A-site and GTPase centre, respectively, before being subjected to a Jiggle Fit in Coot[45]. To model the bound tRNAs, bacterial tRNA (PDB accession code 4V51)[46] was used as a template and modified to the sequence of the most prevalent tRNA for the particular codon from the genomic tRNA database[47]. The atomic models were then modified in Coot v0.8 to agree with the rabbit sequences and optimized for fit to density.

Model refinement and validation. Reciprocal space refinement was carried out in REFMAC v5.8 optimized for electron microscopy maps using external restraints generated by ProSMART and LIBG[45]. The model was refined against amplitudes and phases from the experimental map that were unchanged during the course of refinement. $FSC_{average}$ was monitored during refinement to follow the fit-to-density, and the final model was validated using MolProbity[48] (Extended Data Table 1). The Ramachandran statistics for eRF1 are 93.0% favoured, 1.5% outliers and for ABCE1, 91.1% favoured, 1.9% outliers. Cross-validation against overfitting was calculated as previously described[45,49] (Extended Data Fig. 3c).

30. Shao, S., von der Malsburg, K. & Hegde, R. S. Listerin-dependent nascent protein ubiquitination relies on ribosome subunit dissociation. *Mol. Cell* **50,** 637–648 (2013).
31. Sharma, A., Mariappan, M., Appathurai, S. & Hegde, R. S. in *Protein Secretion* **619,** 339–363 (Humana Press, 2010).
32. Shao, S. & Hegde, R. S. Reconstitution of a minimal ribosome-associated ubiquitination pathway with purified factors. *Mol. Cell* **55,** 880–890 (2014).
33. Bai, X.-C., Fernandez, I. S., McMullan, G. & Scheres, S. H. W. Ribosome structures to near-atomic resolution from thirty thousand cryo-EM particles. *eLife* **2,** e00461 (2013).
34. Li, X. *et al.* Electron counting and beam-induced motion correction enable near-atomic-resolution single-particle cryo-EM. *Nature Methods* **10,** 584–590 (2013).
35. Scheres, S. H. W. Semi-automated selection of cryo-EM particles in RELION-1.3. *J. Struct. Biol.* **189,** 114–122 (2015).
36. Scheres, S. H. W. RELION: Implementation of a Bayesian approach to cryo-EM structure determination. *J. Struct. Biol.* **180,** 519–530 (2012).
37. Scheres, S. H. Beam-induced motion correction for sub-megadalton cryo-EM particles. *eLife* **3,** e03665 (2014).
38. Chen, S. *et al.* High-resolution noise substitution to measure overfitting and validate resolution in 3D structure determination by single particle electron cryomicroscopy. *Ultramicroscopy* **135,** 24–35 (2013).
39. Rosenthal, P. B. & Henderson, R. Optimal determination of particle orientation, absolute hand, and contrast loss in single-particle electron cryomicroscopy. *J. Mol. Biol.* **333,** 721–745 (2003).
40. Kucukelbir, A., Sigworth, F. J. & Tagare, H. D. Quantifying the local resolution of cryo-EM density maps. *Nature Methods* **11,** 63–65 (2014).
41. Voorhees, R. M., Fernandez, I. S., Scheres, S. H. W. & Hegde, R. S. Structure of the mammalian ribosome-Sec61 complex to 3.4 Å resolution. *Cell* **157,** 1632–1643 (2014).
42. Shao, S., Brown, A., Santhanam, B. & Hegde, R. S. Structure and assembly pathway of the ribosome quality control complex. *Mol. Cell* **57,** 433–444 (2015).
43. Pettersen, E. F. *et al.* UCSF Chimera–a visualization system for exploratory research and analysis. *J. Comput. Chem.* **25,** 1605–1612 (2004).

44. Karcher, A., Schele, A. & Hopfner, K. P. X-ray structure of the complete ABC enzyme ABCE1 from *Pyrococcus abyssi*. *J. Biol. Chem.* **283,** 7962–7971 (2008).
45. Brown, A. *et al.* Tools for macromolecular model building and refinement into electron cryo-microscopy reconstructions. *Acta Crystallogr. D* **71,** 136–153 (2015).
46. Selmer, M. Structure of the 70S ribosome complexed with mRNA and tRNA. *Science* **313,** 1935–1942 (2006).
47. Chan, P. P. & Lowe, T. M. GtRNAdb: a database of transfer RNA genes detected in genomic sequence. *Nucleic Acids Res.* **37,** D93–D97 (2009).
48. Chen, V. B. *et al.* MolProbity: all-atom structure validation for macromolecular crystallography. *Acta Crystallogr. D* **66,** 12–21 (2010).
49. Amunts, A. *et al.* Structure of the yeast mitochondrial large ribosomal subunit. *Science* **343,** 1485–1489 (2014).

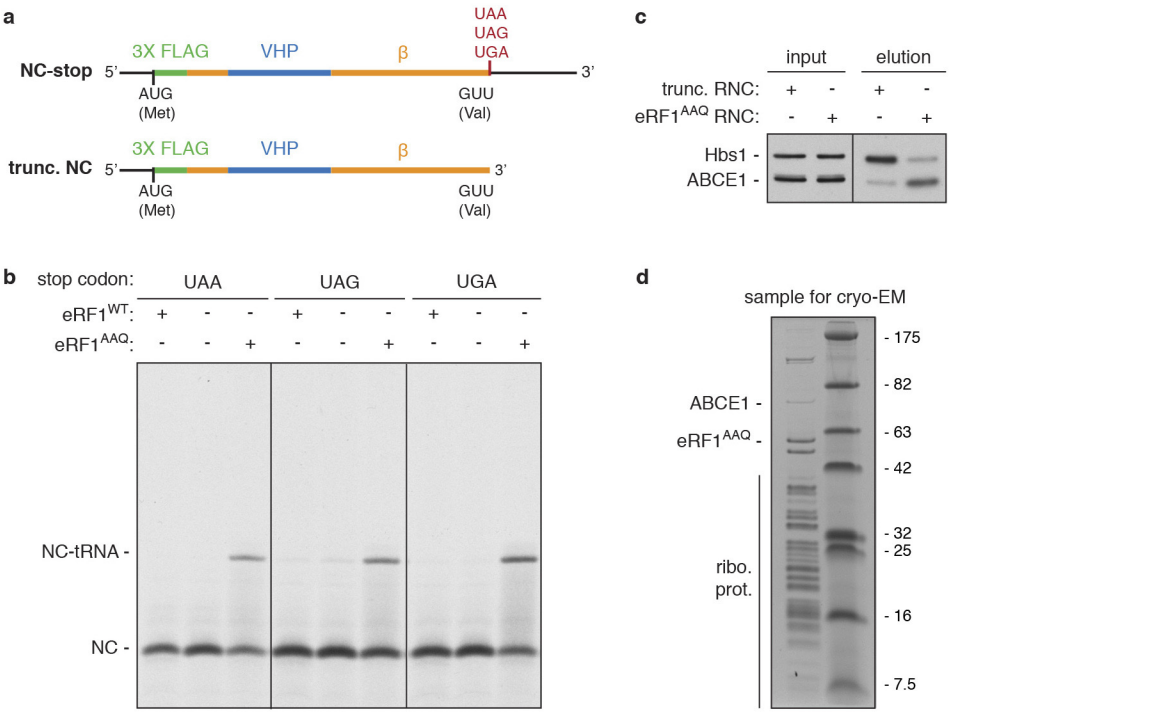

Extended Data Figure 1 | eRF1(AAQ) stalls ribosomes at stop codons. **a**, Line diagrams of mRNA encoding nascent chain (NC) substrates used in this study. The cytosolic portion of human Sec61β (residues 1–68, orange) was modified to contain an N-terminal 3 × Flag tag (green) for affinity purification and the autonomously-folding villin headpiece (VHP, blue) domain. The three stop codons were individually inserted after Val68 of Sec61β to generate substrates for eRF1(AAQ)-mediated stalling, or the mRNA was truncated after the same residue to generate an independently-stalling substrate. **b**, *In vitro* translation reactions of NC-stop substrates containing the indicated stop codon (see panel a) in the presence of [^{35}S]methionine without or with excess eRF1 WT or eRF1(AAQ). Reactions were for 25 min at 32 °C and directly analyzed by SDS–PAGE and auto-radiography. The terminated (NC) and tRNA-associated (NC-tRNA) nascent chain products are indicated. Addition of eRF1(AAQ) selectively prevents peptide hydrolysis when the stop codon is reached. **c**, Anti-Flag affinity purifications of ribosome-nascent chains (RNCs) stalled either by mRNA truncation or at the UAA stop codon with eRF1(AAQ) (see **a**) were immunoblotted for the splitting factors Hbs1 and ABCE1. The different amounts of Hbs1 and ABCE1 co-purified despite identical nascent chain sequences in each RNC complex suggest that eRF1(AAQ) selectively traps ABCE1 on pre-termination complexes. **d**, SDS–PAGE and Coomassie staining of affinity-purified eRF1(AAQ)-stalled ribosome-nascent chains containing the UGA stop codon used for cryo-EM analysis. Bands corresponding to ribosomal proteins, ABCE1, and eRF1(AAQ), which were verified by immunoblotting and mass spectrometry (data not shown), are indicated.

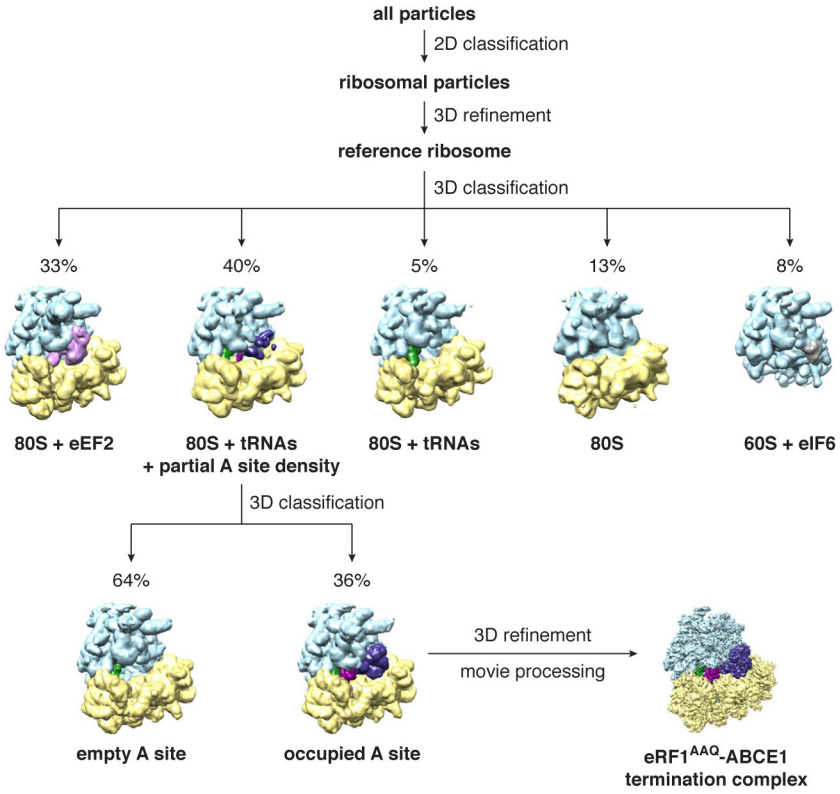

Extended Data Figure 2 | *In silico* 3D classification scheme for cryo-EM data sets. Particles extracted from automated particle picking in RELION were subjected to 2D classification. Non-ribosomal particles were discarded and the remaining particles were combined for a 3D refinement. The resulting map was used as a reference for 3D classification, which typically isolated 5 distinct classes of ribosomal complexes with the indicated distributions. Classes containing 80S ribosomes with canonical P- and E-site tRNAs and weak factor density in the A-site (~40%) were combined and subjected to another round of 3D classification for A-site occupancy. Approximately one-third of this population contained strong density for eRF1(AAQ) and ABCE1. These particles were combined for subsequent 3D refinement and movie processing. All four data sets (two for the UAA stop codon and one each for the UAG and UGA stop codons) were processed similarly. The eRF1(AAQ)–ABCE1-containing particles of the two UAA data sets after the two rounds of classification were combined for refinement to yield the final map.

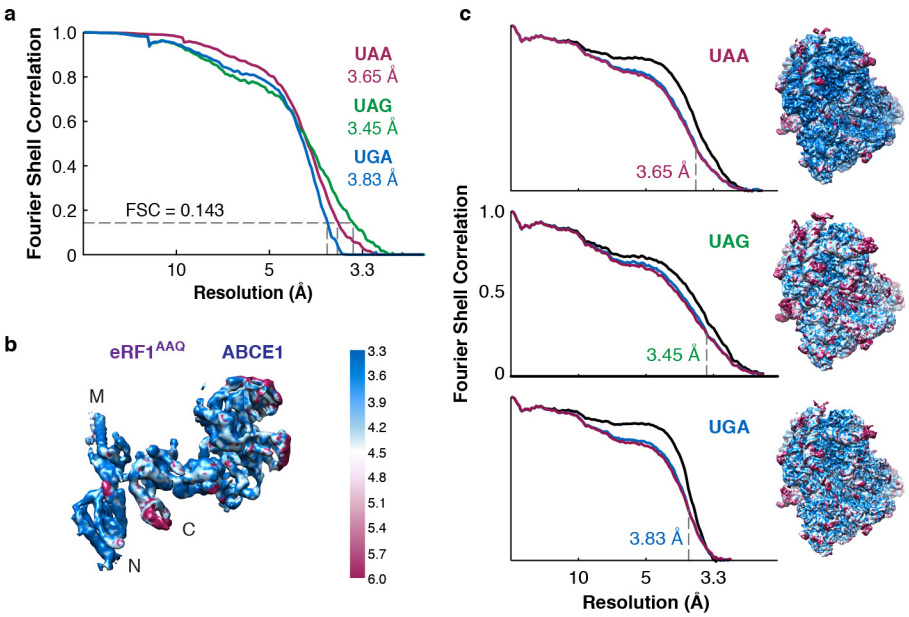

Extended Data Figure 3 | Quality of maps and models. **a**, Fourier shell correlation (FSC) curves for the electron microscopy maps of each termination complex containing the indicated stop codon. **b**, Isolated eRF1(AAQ)–ABCE1 density from the UAA termination complex map coloured by local resolution. **c**, Fit of models to maps. FSC curves calculated between the refined model and the final map (black), and with the self- (blue) and cross-validated (magenta) correlations for each stop codon complex. The electron microscopy map of each termination complex coloured by local resolution (as in **b**) is displayed next to the corresponding curves.

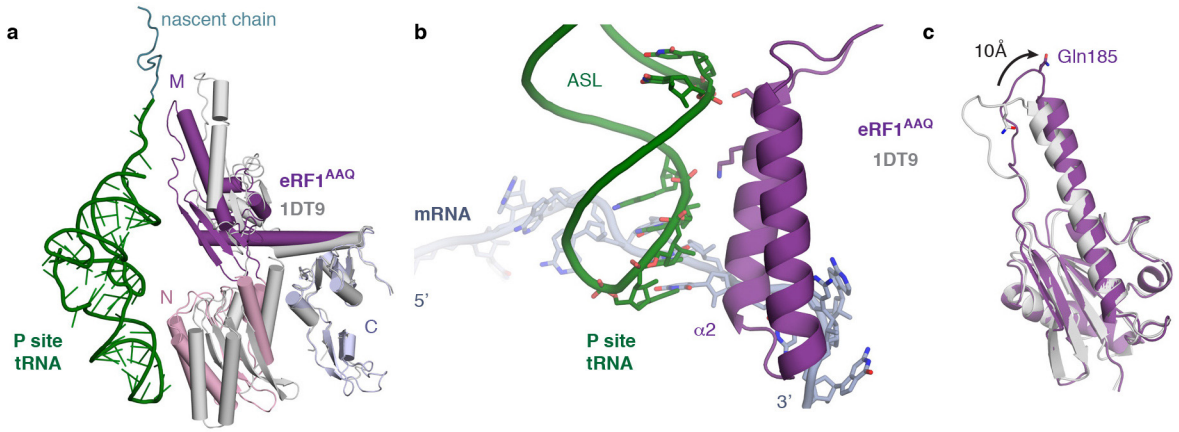

Extended Data Figure 4 | eRF1(AAQ) interactions within the termination complex. **a**, Comparison of ribosome-bound eRF1(AAQ) (coloured by domain) with the crystal structure of eRF1 (PDB accession code 1DT9, grey) superposed on the C domain. Both the N and M domains of eRF1 rotate upon stop codon recognition on the ribosome. The P-site tRNA (green) and nascent chain (teal) are shown for orientation. **b**, Interaction of helix α2 of the N domain of eRF1(AAQ) (purple) with the anticodon stem loop (ASL) of the P-site tRNA (green). **c**, Superposition of the eRF1(AAQ) M domain (purple) with the eRF1 crystal structure (PDB accession code 1DT9) showing a 10 Å movement of the GGQ-loop to accommodate within the peptidyl transferase centre.

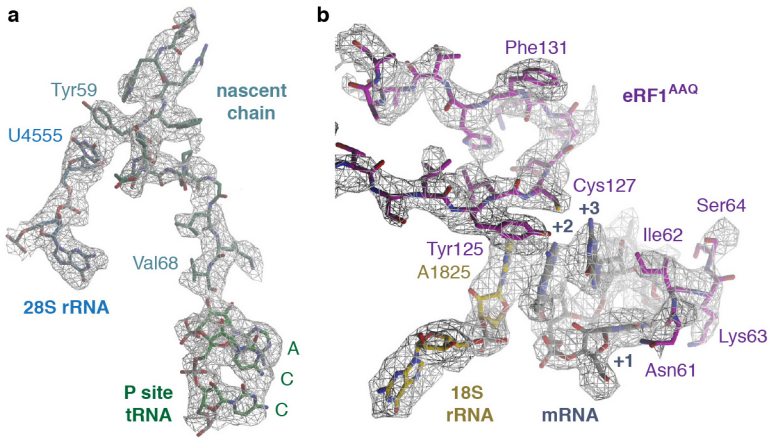

Extended Data Figure 5 | Examples of map densities. **a**, Density (from the UAG-containing termination complex) for the nascent chain (teal) attached to the CCA end of the P-site tRNA (green) is of sufficient resolution to model the defined sequence of the C-terminal end of the programmed nascent chain. This provides additional verification that the termination complexes are stalled at Val68 of Sec61β (human numbering) with the stop codon in the A-site (see also Extended Data Fig. 1a). A stacking interaction between an aromatic residue of the nascent chain and U4555 (blue) lining the ribosomal exit tunnel can also be observed. **b**, Densities for the interactions between the UAG stop codon (grey), a portion of h44 of 18S rRNA (yellow) and the YxCxxxF and NIKS motifs of eRF1(AAQ) (purple). The invariant isoleucine of the NIKS motif provides a hydrophobic base for the stacking of the +2 and +3 bases of the stop codon with A1825. Unlike the tyrosine and cysteine residues of the YxCxxxF motif, the phenylalanine does not contribute to stop codon recognition, but to the hydrophobic packing of the eRF1 N domain.

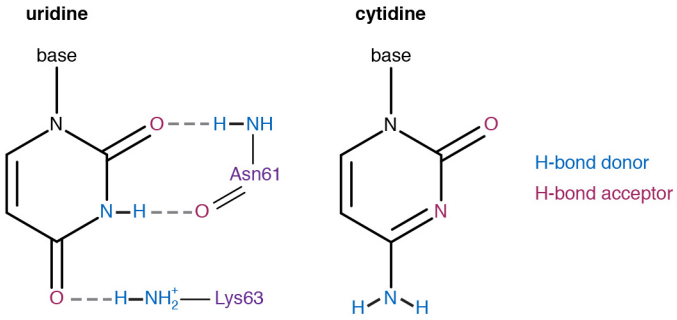

Extended Data Figure 6 | Hydrogen bonds specify for uridine at the +1 position. Chemical diagrams of uridine and cytidine with hydrogen bond donors (blue) and acceptors (magenta) indicated. Two of the three hydrogen bonds that uridine forms with Asn61 and Lys63 of the NIKS motif of eRF1(AAQ) (purple) are not possible with cytidine (see also Fig. 4a).

Extended Data Table 1 | Refinement and model statistics

	UAA	UAG	UGA
Data Collection			
Particles	49,979	20,515	22,058
Pixel size (Å)	1.34	1.34	1.34
Defocus range (μm)	1.1-5.9	0.7-4.1	0.7-3.8
Defocus mean (μm)	3.2	2.4	2.3
Voltage (kV)	300	300	300
Electron dose (e- $Å^{-2}$)	30	30	30
Model composition			
Non-hydrogen atoms	226,532	226,533	226,533
Protein residues	12,676	12,676	12,676
RNA bases	5,820	5,820	5,820
Ligands (Zn^{2+}/Mg^{2+}/ADP)	8/197/2	8/197/2	8/197/2
Refinement			
Resolution (Å)	3.65	3.45	3.83
Map sharpening B-factor ($Å^2$)	-81.7	-50.6	-82.7
Average B factor ($Å^2$)	105.8	87.4	93.5
$FSC_{average}$	0.85	0.84	0.88
$FSC_{average}$ (eRF1)	0.70	0.64	0.74
$FSC_{average}$ (ABCE1)	0.71	0.62	0.75
R.m.s. deviations			
Bond lengths (Å)	0.006	0.006	0.008
Bond angles (°)	1.19	1.22	1.40
Validation			
Molprobity score	2.7 (93^{rd} percentile)	2.8 (89^{th} percentile)	3.0 (89^{th} percentile)
Clashscore, all atoms	5.2 (100^{th} percentile)	6.2 (97^{th} percentile)	8.2 (97^{th} percentile)
Good rotamers (%)	88.2	87.5	86.4
Ramachandran plot			
Favored (%)	87.0	85.8	83.5
Outliers (%)	3.3	3.5	4.2
Validation (RNA)			
Correct sugar puckers (%)	96.5	93.4	96.0
Good backbone conformations (%)	68.2	66.8	65.8